ISSN (Print) 1226-1750
ISSN (Online) 2233-6656
Journal of Magnetics 30(4), 510-518 (2025) https://doi.org/10.4283/JMAG.2025.30.4.510

Design and Analysis of a 2-Way Microspeaker with Separated Dual Coils for Improved Acoustic Performance

Kyeong-Tak Park[1], Dan-Ping Xu[2], Ji-Hun Park[1], and Sang-Moon Hwang[1]*

[1]*School of Mechanical Engineering, Pusan National University, Busan 46241, Republic of Korea*
[2]*School of Mechatronic Engineering and Automation, Shanghai University, Shanghai 200444, China*

(Received 18 February 2025, Received in final form 1 December 2025, Accepted 3 December 2025)

The purpose of this study is to determine the optimal microspeaker design for increasing low and mid-frequency sound pressure level (SPL) performance. This is because recent changes in the shape of smartwatches have allowed for the use of larger microspeakers, which can improve acoustic performance. This study aims to determine the optimal microspeaker design for increasing the low- and mid-frequency sound pressure level (SPL) performance based on three new microspeaker designs. The prototype has a single-coil design, whereas the three new types are dual-coil designs with separate woofer (WF) and tweeter (TW) units. This study identified the optimal design by comparing all types of SPL using an electromagnetic–mechanical–acoustic (E-M-A) coupling analysis method. According to the analysis results, Type 2, with a 7:3 WF-to-TW size ratio, significantly improved the SPL in the mid-frequency range, with a small increase in SPL in the low-frequency range. Consequently, a Type 2 sample was fabricated to validate the analysis results. The experimental results confirmed the improved SPL performance and validated the simulation result.

Keywords : Microspeaker, Sound pressure level, Two-way microspeaker, Magnetic circuit design, Magnetic flux density and Electromagnetic analysis

1. Introduction

Concerning the acoustic performance of mainstream wearable devices [1], smartwatches, known for their intelligent functions, such as health monitoring, notifications, and phone calls, have gained significant popularity. However, the small size of the microspeakers in smartwatches limits their acoustic capabilities. In a previous study, Jiang et al. proposed a microspeaker design for smartwatches featuring a novel diaphragm material to improve the low-frequency response and waterproofing performance while maintaining a consistent mid-frequency performance [2]. However, this study focused on low- and mid-frequency performance.

Smartwatches typically feature a watch speaker positioned on the side of the device. As shown in Fig. 1(a), in a circular frame design, this placement results in unused space, leading to inefficient space utilization. To address this inefficiency, a rectangular frame design is adopted, as shown in Fig. 1(b), wherein positioning the speaker in the corner allows for more efficient use of space, which helps accommodate a larger speaker size compared to the circular frame. The main objective is to improve the mid-frequency range sound pressure level (SPL) while also seeking enhancements in the low-frequency range. Therefore, a novel magnetic circuit design is required to enhance the acoustic performance. Recent studies have focused on optimizing the magnetic circuit topology of linear permanent magnet machines [3] and direct-drive

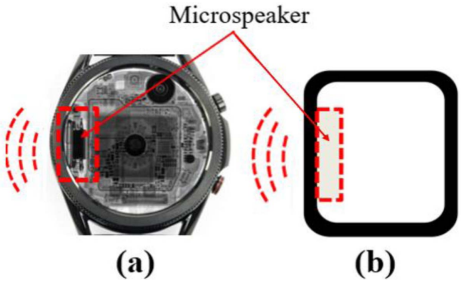

Fig. 1. (Color online) Comparison of smartwatch form factors: (a) conventional circular frame resulting in unused space, and (b) rectangular frame allowing efficient space utilization for larger speaker placement.

*Corresponding author: Tel: +82-510-3204
Fax: +82-510-3204, e-mail: shwang@pusan.ac.kr

actuators [4] to maximize electromagnetic force. Research on enhancing power density through structural optimization has also been actively conducted [5]. Furthermore, accurate prediction of magnetic field behavior using numerical modeling [6] and analysis of magnetic coupling characteristics [7] are considered essential for high-performance electromagnetic system design.

2. Prototype and Material Properties

Fig. 2 shows the full model, half model, and exploded view of the prototype, which comprises the center diaphragm (CDP) and side diaphragm (SDP). The upper and lower frames provide structural support. The magnetic circuit consists of a coil, ferromagnetic material, and a permanent magnet. The terminal and suspension facilitate the current flow to the coil and provide mechanical support. The frame is composed of polycarbonate (PC). The CDP is composed of aluminum, while the SDP is made of liquid silicone rubber (LSR).

As shown in Fig. 3, the magnetic circuit of the prototype consists of a yoke, top plate, permanent magnet, and coil. The yoke and top plate are made of steel plate cold commercial (SPCC), a nonlinear ferromagnetic material. The coil is made of Daikoku high-tension (DHT) wire. The direct-current resistance (DCR) of the coil is 8.5 Ω, and the total coil length is 1317.8 mm. A neodymium iron boron (NdFeB) permanent magnet with a 1.45 T remanence and grade N52H is used. Table 1 presents the mechanical material properties of the prototype.

A permanent magnet generates the magnetic field within the magnetic circuit of the microspeaker. This magnetic field, formed by the permanent magnet and a ferromagnetic material, interacts with a coil placed in the

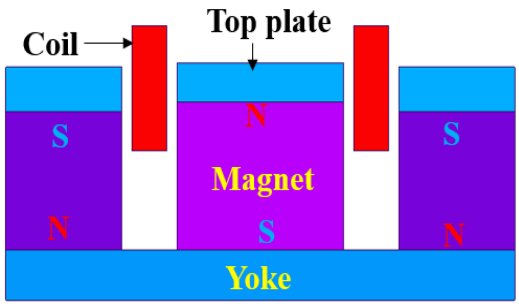

Fig. 3. (Color online) Cross-sectional view of magnetic circuit of the prototype, illustrating the arrangement of key components of magnetic circuit.

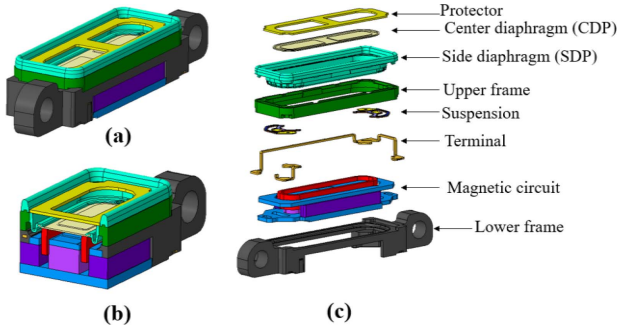

Fig. 2. (Color online) Structural configuration of the prototype: (a) full model, (b) half model, and (c) exploded view.

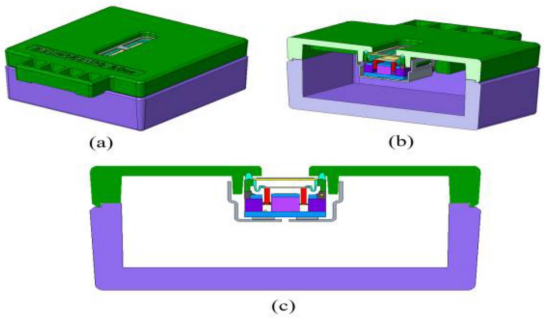

Fig. 4. (Color online) Configuration of the prototype mounted in a 3cc testing box: (a) full model, (b) half model, and (c) cross-sectional view.

Table 1. Mechanical material properties of the prototype.

Part	Material	Density [kg/m^3]	Young's modulus [GPa]	Poisson's ratio
Side diaphragm	Liquid silicone rubber	1100	0.012	0.40
Center diaphragm	Aluminum	2700	70	0.28
Coil	Daikoku High Tension	5320	110	0.35
Yoke & TP	SPCC	7821	207	0.29
Magnet	Neodymium iron boron	7394	41.4	0.30
Suspension	Polyimide (PI) film	2110	2.5	0.34
Frame	Polycarbonate	1200	2.3	0.38

air gap. When electric current flows through the coil, it experiences a Lorentz force that drives the microspeaker. This force causes the coil to vibrate, and the vibration transmit to the attached diaphragm. The movement of the diaphragm creates pressure variations in the surrounding air, generating sound waves that people perceive as sound. Fig. 4 shows the prototype in the 3cc testing box—used to measure its SPL.

3. Analysis Method

3.1. Electromagnetic analysis

The electromagnetic domain consists of a yoke, top plate, permanent magnet, and coil. The voltage equation for the microspeaker, which includes the inductance and back electromotive force (V_{bemf}) terms [8], is given by Eq. (1)

$$V_e = iR_e + L_e\frac{di}{dt} + V_{bemf} \tag{1}$$

$$V_{bemf} = B_{avg}Lv \tag{2}$$

where V_e, i, R_e, L_e, di/dt, v, B_{avg} and L are the input voltage, electrical current, DCR, inductance, partial derivative of current with respect to time, mechanical velocity of the coil, magnetic flux density on the coil and total coil length, respectively.

The Lorentz force is given by Eq. (3) [9]. As shown in Eqs. (2) and (3), V_{bemf} and $F_{Lorentz}$ share the $B_{avg}L$ term. This term, commonly referred to as the force factor (K_f), plays a crucial role in coupling the electromagnetic and mechanical domains, essentially quantifying the efficiency of the conversion of electrical energy into mechanical energy.

$$F_{Lorentz} = B_{avg}Li \tag{3}$$

$$K_f = B_{avg}L \tag{4}$$

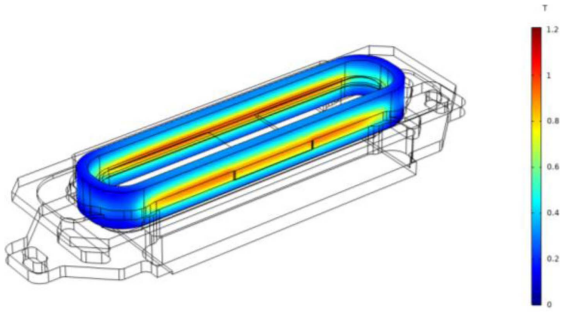

Fig. 5. (Color online) Electromagnetic field FEM simulation results for the prototype, displaying the magnetic flux density distribution on coil.

Electromagnetic analysis was conducted using the COMSOL Multiphysics software [10]. Fig. 5 shows the simulation results for the prototype. B_{avg} was calculated to be 0.468 T.

3.2. Mechanical analysis

The governing equation for this mechanical system is the forced vibration equation as shown in Eq. (5) [11]. The forced vibration equation of the microspeaker can be solved by using the finite element method (FEM).

$$[M]\{a\} + [C]\{v\} + [K]\{x\} = \{F\} \tag{5}$$

where [M], {a}, [C], {v}, [K], {x}, and {F} denote the mass matrix, acceleration vector, damping matrix, velocity vector, stiffness matrix, displacement vector, and force vector, respectively. The force vector is be by {F} (Eq. (6)), i.e., the sum of $F_{Lorentz}$ and $F_{pressure}$ [1].

$$\{F\} = \{F_{Lorentz}\} + \{F_{pressure}\} \tag{6}$$

$$F_{pressure} = S_d\Delta p \tag{7}$$

where S_d and Δp are the effective radiation area of SPK and the pressure difference between upper and lower surfaces of the diaphragm, respectively.

By solving the undamped free vibration equation, the natural frequency (w_n) can be calculated using Eq. (8). In the microspeaker, total stiffness (K_{total}) consists of K_{Added} and K_{mech} as shown in Eq. (9) [12]. K_{Added} is shown in Eq. (10) [13]. K_{mech} is the mechanical stiffness of the SPK unit.

$$w_n = \sqrt{\frac{K_{total}}{M}} \tag{8}$$

$$K_{total} = K_{mech} + K_{Added} \tag{9}$$

$$K_{Added} = \frac{\rho_0 c^2 s_d^2}{V_{cc}} \tag{10}$$

where ρ_0, c, and V_{cc} represent the air density, speed of sound in air, and air volume of the testing box. The effective radiation area (S_d) is defined as the mechanical-acoustic coupling factor, which quantifies the amount of the mechanical energy generated by the SPK that can be effectively radiated as sound waves into the surrounding air.

3.3. Electromagnetic–mechanical–acoustic coupling analysis [14]

The governing acoustic equation describing the propagation of sound waves in air is 3D linearized acoustic wave equation. This equation is a form of the wave equation and can be written as follows:

$$\nabla^2 p - \frac{1}{c^2}\frac{\partial^2 p}{\partial t^2} = 0 \tag{11}$$

where p, ∇^2, and $\frac{\partial^2 p}{\partial t^2}$ are the sound pressure in 3D space, Laplacian operator, and second partial derivative of the sound pressure with respect to time, respectively. Solving the 3D linearized acoustic wave equation using FEM allows the simulation of the behavior of sound waves in complex 3D geometries, such as in microspeakers.

The volume velocity of the SPK, which refers to the volumetric flow rate of air displaced by the movement of the SPK diaphragm, represents the amount of air pushed or pulled by the diaphragm as it vibrates in response to an electrical audio signal. The volume velocity U can be calculated using Eq. (12).

$$U = S_d v \tag{12}$$

The relationship between volume velocity and sound pressure can be described using Eq. (13):

$$p = \rho_0 c U. \tag{13}$$

The SPL of an SPK relates the acoustic power output of the speaker to the SPL at a specific distance from the SPK, as shown in Eq. (14).

$$SPL = 20 log_{10}\left(\frac{p_{rms}}{p_{ref}}\right) \tag{14}$$

where p_{rms} denotes the root-mean-square sound pressure at the measured position. p_{ref} is the reference sound pressure, i.e., is the quietest sound that a typical human ear can detect under standard atmospheric conditions. The reference sound pressure is approximately 20 μPa. Two analysis methods were used to solve the coupling problem of E-M-A domain. Fig. 6 shows schematics of two analytical methods.

The first method, shown in Fig. 6(a), uses a combination of the lumped parameter method (LPM) and the finite element method (FEM), resulting in more accurate analysis results at high frequencies, considering the acoustic structure effect.

The other method, shown in Fig. 6(b), applies the LPM to three domains, considering the acoustic back volume impedance (Z_{bc}) and radiation impedance (Z_r). Table 2 summarizes the interpretation methods for each approach.

4. SPL Experiment

4.1. Experimental setup

The measurement setup and prototype sample are

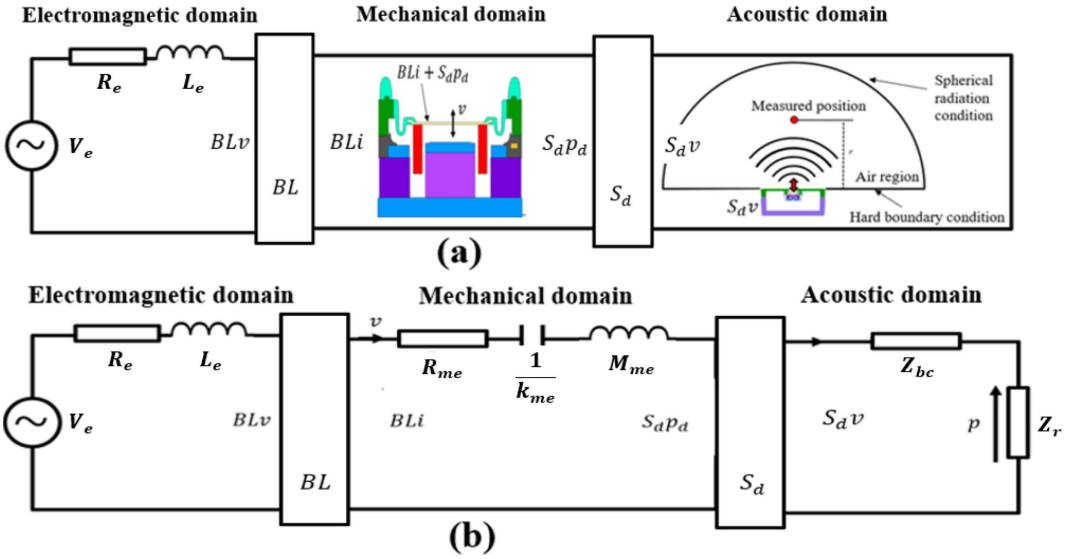

Fig. 6. (Color online) Schematics of E-M-A coupling analysis methods: (a) Method #1 combining LPM and FEM and (b) Method #2 using full LPM.

Table 2. Comparison of electromagnetic, mechanical, and acoustic domain analysis in Method #1 and Method #2.

	Electromagnetic domain	Mechanical domain	Acoustic domain
Method #1	Lumped Parameter Method	Finite Element Method	
Method #2		Lumped Parameter Method	

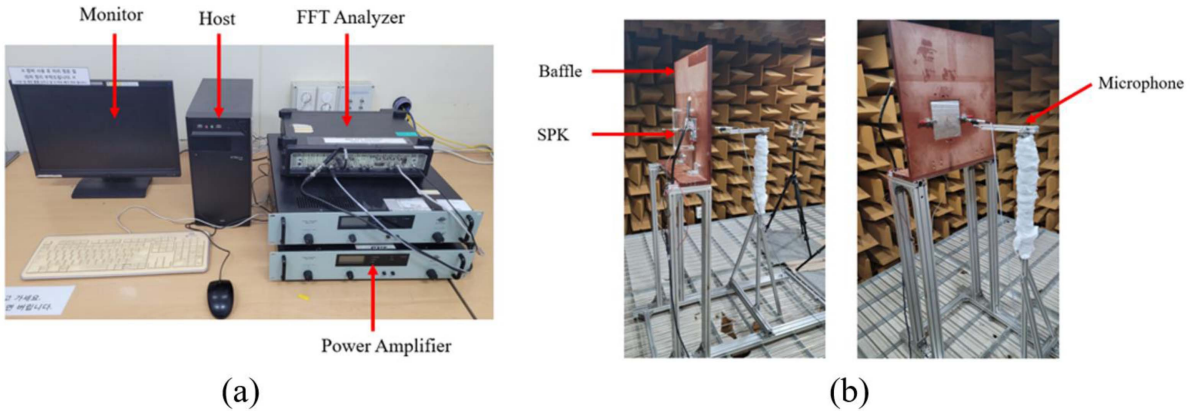

Fig. 7. (Color online) Experimental setup for SPL measurement: (a) FFT analyzer, power amplifier, monitor, and host; (b) measurement arrangement inside the anechoic chamber with a baffle, SPK, and microphone.

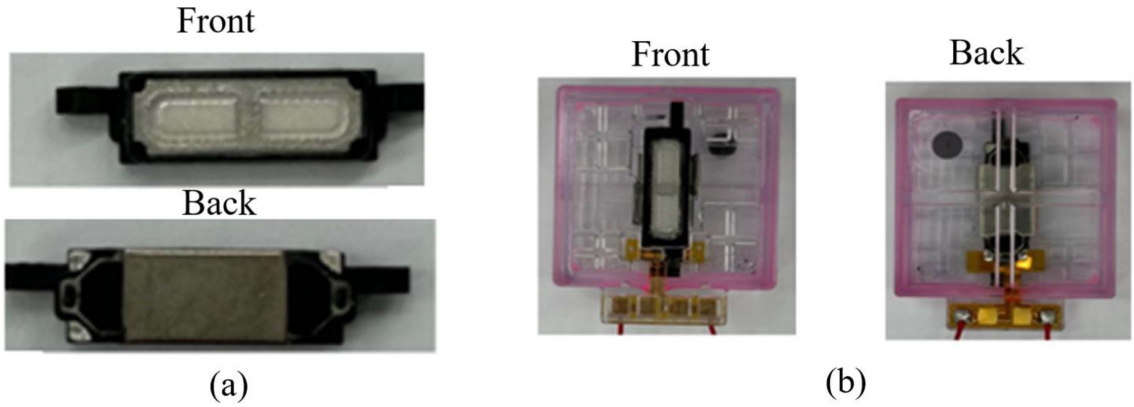

Fig. 8. (Color online) Fabricated prototype samples: (a) front and back views of the speaker unit, and (b) the unit assembled within the testing box.

shown in Figs. 7 and 8, respectively. Fig. 7 shows the fast Fourier transform (FFT) analyzer, power amplifier, host, monitor, anechoic chamber, baffle, and microphone. Front and back views of the sample in the testing box are shown in Fig. 8. The SPL of the SPK in the testing box was measured accurately using a microphone placed at a fixed distance of 10 cm from the baffle surface. This standardized measurement setup ensures reliable and consistent results. Inputting a sinusoidal current signal into the microspeaker coil, generates sound waves measured using a microphone. The sound wave data can be analyzed using an FFT analyzer to determine the frequency response of the SPK.

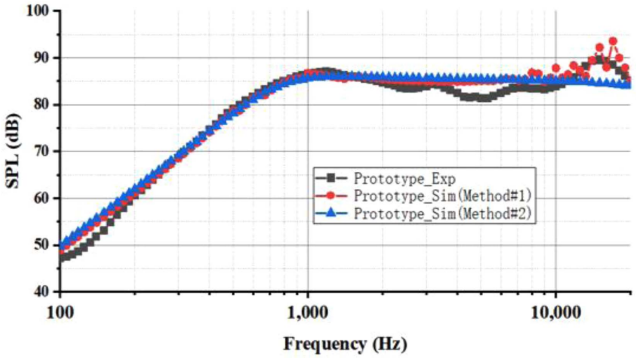

Fig. 9. (Color online) Comparison of experimental and simulated SPL results for the prototype, validating the accuracy of the proposed analysis methods.

4.2. SPL verification

Fig. 9 shows the experimental data measured in an anechoic chamber and the results obtained using Methods #1 and #2. The analysis demonstrated a strong correlation between the experimental results and both methods in the low and mid-frequency ranges. Although Method #1 provides accurate results across the entire frequency range, it requires 180 min for analysis. In contrast, Method #2 completes the analysis in only 5 min. Method #2 offers a good approach for predicting SPL, requiring only a magnetic circuit and diaphragm modeling. This

simplified process makes it particularly advantageous for this study, which involves evaluating several microspeaker models to enhance the low and mid-frequency SPL. Therefore, Method #2 was employed for efficient and iterative design and analysis.

5. New Microspeaker Designs

5.1. New magnetic circuit design

Jiang et al. proposed an inserted dual-coil microspeaker design, utilizing a woofer (WF) and tweeter (TW) unit to improve the SPL in the mid-frequency range, as shown in Fig. 10(a) [14]. The prototype dimensions 13.7 × 5.0 × 2.15 mm, as shown in Fig. 10(b). Considering a smartwatch's width directly affects its thickness, increasing its size is challenging. Therefore, the dimensions of the new dual-coil design were set to 19.2 × 6.5 × 3 mm. However, this size makes it difficult to apply the inserted design. Thus, this study employed a separated dual-coil design for effective size utilization, as shown in Fig. 10(c).

5.2. New diaphragm structure

Three new dual-coil microspeaker designs with varying WF and TW unit length ratios, as illustrated in Fig. 11. The percentages represent the ratios of WF and TW unit lengths to the total length. The inner and outer magnet sizes were adjusted for each designated speaker length. Consequently, this adjustment requires changes in the coil specifications. Table 3 presents the detailed coil specifi-

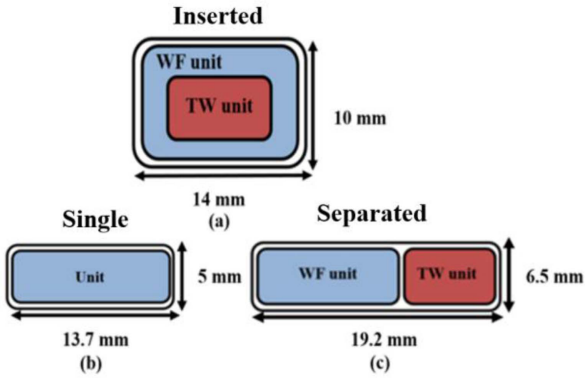

Fig. 10. (Color online) Coil configurations considering spatial constraints: (a) conventional inserted dual-coil, (b) single-coil, and (c) the proposed separated coil design.

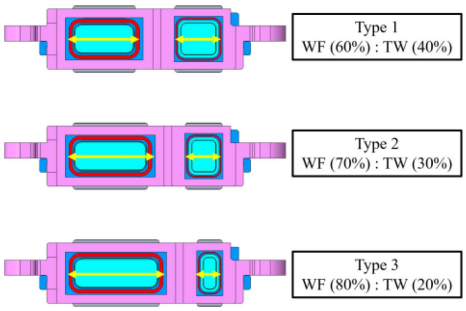

Fig. 11. (Color online) Design specifications for the three proposed dual-coil types characterized by varying woofer (WF) to tweeter (TW) length ratios.

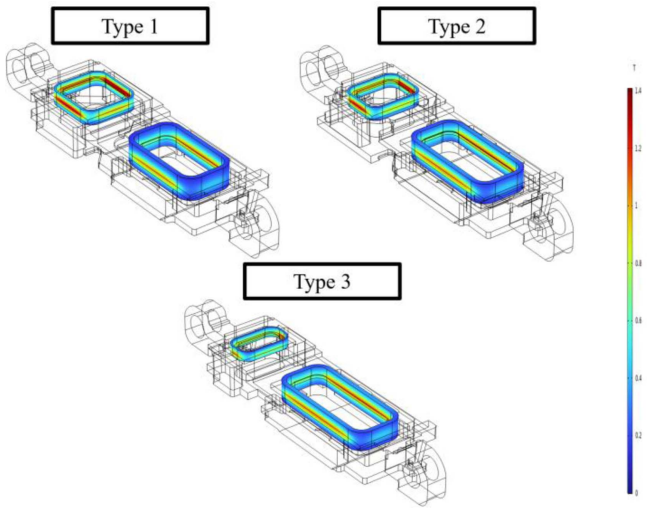

Fig. 12. (Color online) Electromagnetic field FEM simulation results for three types, displaying the magnetic flux density distribution on coil.

Table 3. Coil specifications for the prototype and three proposed types, including diameter, total length, mass and force factor for both Woofer (WF) and Tweeter (TW) units.

Parts	WF parts				TW parts			
Parameters	Diameter [mm]	Length [mm]	Mass [mg]	Force factor [N/A]	Diameter [mm]	Length [mm]	Mass [mg]	Force factor [N/A]
Prototype	0.070	1317.8	24.2	0.617	-	-	-	-
Type 1	0.075	1362.2	23.0	0.594	0.055	498.9	7.20	0.336
Type 2	0.077	1351.2	24.0	0.654	0.051	428.8	5.37	0.269
Type 3	0.079	1423.0	26.5	0.718	0.045	319.1	2.97	0.184

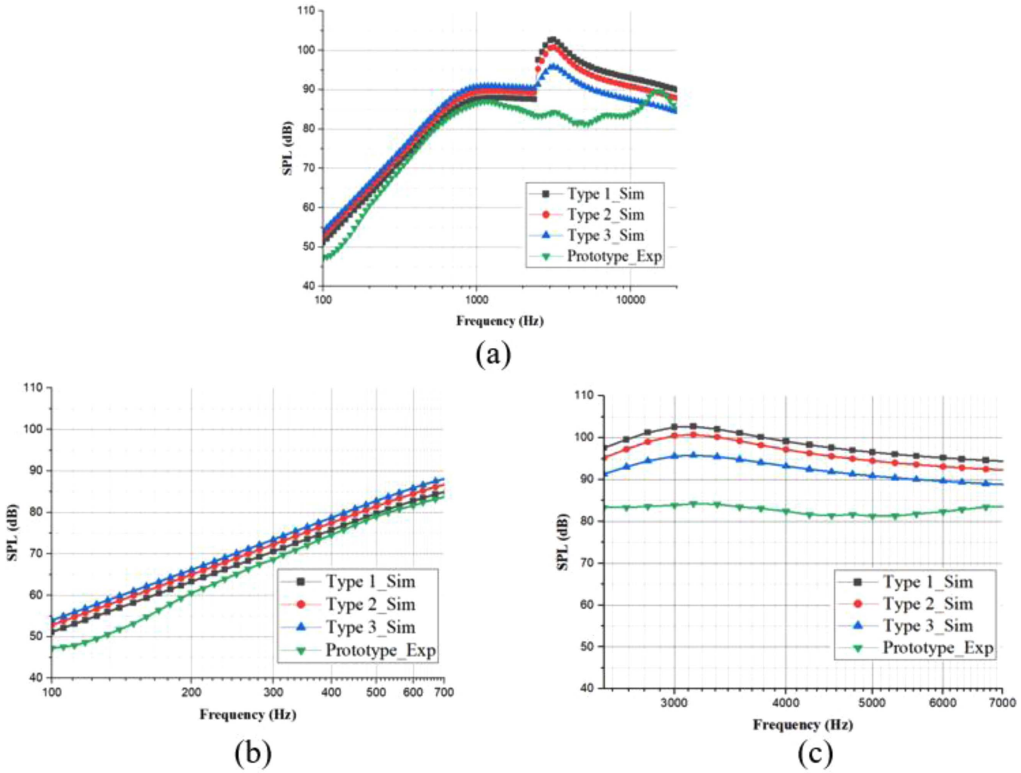

Fig. 13. (Color online) Comparison of the simulated SPL results for all types: (a) full audible frequency range (100 Hz-20 kHz), (b) low-frequency range (100 Hz-700 Hz), (c) mid-frequency range (2.5 kHz-7 kHz).

cations, including diameter, total length, mass, and force factor for both the Woofer (WF) and Tweeter (TW) units of the prototype and the three proposed types. The electromagnetic simulation results for the three types are shown in Fig. 12.

To take advantage of the dual-coil design, the WF operates in the frequency range of 100 Hz to 2500 Hz, while the TW operates in the frequency range of 2.5 kHz to 20 kHz. The input voltage is 3.63 Vrms.

6. Result and Discussion

Fig. 13 presents the comparison between the experimental results of the prototype and the simulation results of the three proposed types. Fig. 13(a) displays the SPL across the entire audible range (100 Hz to 20 kHz). To provide a detailed analysis, magnified views of the low-frequency range (100 Hz to 700 Hz) and mid-frequency range (2.5 kHz to 7 kHz) are shown in Figs. 13(b) and 13(c), respectively.

As observed in Fig. 13(b), Type 3 exhibited the highest SPL in the low-frequency range, followed by Types 2 and 1. Conversely, in the mid-frequency range shown in Fig. 13(c), Type 1 exhibited the highest SPL, followed by Types 2 and 3. Table 4 summarizes the average SPL for the low- and mid-frequency ranges for all types.

In the low-frequency range, Type 3, featuring the largest WF size, achieves an SPL of 71.33 dB, representing a 5.53 dB increase compared to the prototype, followed by Type 2, with a 4.30 dB increase, and Type 1, with a 2.59 dB increase. In the mid-frequency range, Type 1 exhibits the highest SPL, with a 15.45 dB improvement over the prototype, followed by Type 2, with a 13.40 dB increase, and Type 3, with a 9.41 dB increase.

These results indicate that the SPL tends to change in the same direction as the unit size because both the

Table 4. Comparison of average SPL in low- (100-700 Hz) and mid-frequency (2.5-7 kHz) ranges between simulations and experiments.

Types	Low-frequency [dB] (100~700 Hz)	Mid-frequency [dB] (2.5~7 kHz)
Prototype_Exp	65.80	82.79
Type 1_Sim	68.39 (+ 2.59 dB)	98.24 (+ 15.45 dB)
Type 2_Sim	70.10 (+ 4.30 dB)	96.19 (+ 13.40 dB)
Type 3_Sim	71.33 (+ 5.53 dB)	92.20 (+9.41 dB)
Type 2_Exp	68.27 (+2.47 dB)	95.10 (+12.31 dB)

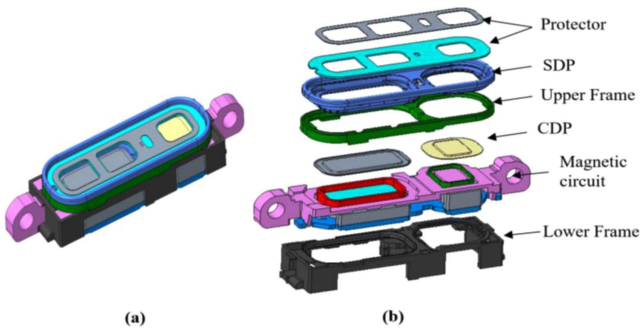

Fig. 14. (Color online) Structural configuration of the Type2: (a) full model and (b) exploded view.

effective radiation area and force factor increase with size. However, considering this observation only reveals the trend of SPL increase or decrease without providing specific values, further analysis was conducted on these three models.

Considering the objective of this study, i.e., to improve both the low- and mid-frequency SPL, Type 2 emerged as the most suitable choice, demonstrating a balanced enhancement across both frequency ranges.

7. Experiment and Verification

Fig. 14 shows the full model and exploded view of the Type 2. Fig. 15 shows the fabricated sample based on the Type 2 design. A comparison of the experimental and simulated SPL data is shown in Fig. 16. The results demonstrate good agreement between the simulation and measurement across both the low- and mid-frequency ranges. Table 4 also lists the average of SPL in the low- and mid-frequency ranges for the simulation and experimental data of Type 2.

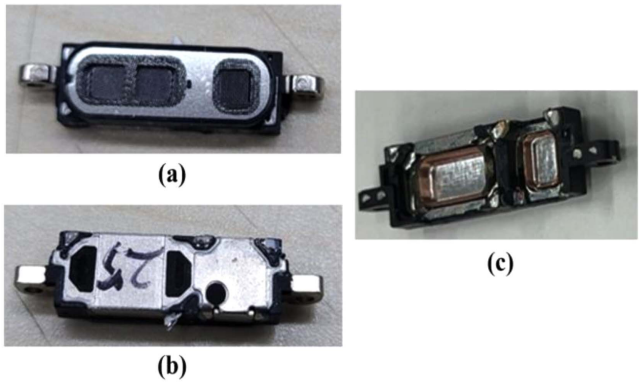

Fig. 15. (Color online) Fabricated sample based on the Type 2 design: (a) top view, (b) back side view, and (c) inside view without yoke.

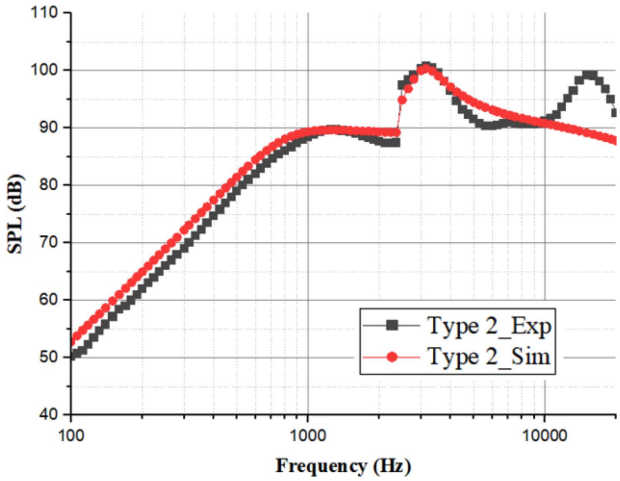

Fig. 16. (Color online) Experimental verification of the Type 2: Comparison of simulated and measured SPL across the full frequency range (100 Hz-20 kHz).

8. Conclusion

This study investigated methods to significantly enhance the low- and mid-frequency performance of microspeakers in smartwatches, particularly in the mid-range, by capitalizing on the increased design space afforded by the transition from circular to rectangular watch shapes. Based on the conventional one-coil design of the prototype, a novel separated dual-coil design was implemented in the proposed configurations.

In this study, an E-M-A coupling analysis method was used to predict SPL of a microspeaker. The validity and reliability of this method were confirmed through comprehensive comparisons with experimental measurements, demonstrating its effectiveness in capturing the SPL of the microspeaker across both low- and mid-frequency ranges. Three types were developed and characterized by variations in unit size. Type 2, featuring an approximate 7:3 WF-to-TW ratio, emerged as the most effective for fulfilling the research objectives.

A sample based on the Type 2 design was fabricated and tested to validate the simulation results. The experimental data exhibited reasonable consistency with the simulation results in both the low- and mid-frequency ranges, thus confirming the accuracy of the E-M-A coupling analysis.

Hence, this study presents a novel approach to microspeaker design with enhanced low- and mid-frequency performance and contributes a valuable advancement to the field of audio engineering by demonstrating the effectiveness of E-M-A coupling analysis in predicting and optimizing microspeaker behavior.

References

[1] K. H. Park, Z. X. Jiang, and S. M. Hwang, Appl. Sci. **10**, 8902 (2020).
[2] Z. X. Jiang, K. H. Park, and S. M. Hwang, Sensors and Actuators A: Physical **338**, 113452 (2022)
[3] G. Rong and H. Wei, J. Magn. **28**, 268 (2023).
[4] S. Z. Chen, Z. Y. Shi, Z. Z. Tian, J. Xu, and Q. J. Wang, J. Magn. **30**, 91 (2025).
[5] J. K. Lee and S. J. Moo, J. Magn. **29**, 135 (2024).
[6] A. Mohammed, J. Magn. **29**, 42 (2024).
[7] J. Y. Kim, H. J. Lee, J. H. Oh, K. S. Yoon, J. H. Lee, and I. K. Cho, J. Magn. **29**, 338 (2024).
[8] D. P. Xu, Y. W. Jiang, H. K. Kim, J. H. Kwon, and S. M. Hwang, IEEE Access. **5**, (2017) pp. 8930-8939.
[9] I. Shahosseini, L. Elie, J. Moulin, E. Martincic, M. Woytasik, and G. Lemarquand, IEEE Sens. J. **13**, 273 (2013).
[10] M. W. Kennedy, S. Akhtar, J. A. Bakken, and R. E. Aune, Proc. COMSOL Users Conf. 1-9 (2011).
[11] S. S. Rao, Mechanical Vibrations, sixth ed, Pearson Education, London (2017) pp. 259-269.
[12] Z. X. Jiang, J. H. Park, D. P. Xu, and S. M. Hwang, Appl. Sci. **13**, 1018 (2023).
[13] P. Sun, D. P. Xu, and S. M. Hwang, Journal of Mechanical Science and Technology **28**, 1623 (2014).
[14] Z. X. Jiang, D. P. Xu, K. T. Park, and S. M. Hwang, Sensors and Actuators A: Physical **365**, 114914 (2024).